Numerical Two-Phase Simulations of Alkaline Water Electrolyzers

ECS Transactions, 112 (4) 419-431 (2023)
10.1149/11204.0419ecst ©The Electrochemical Society

Numerical Two-Phase Simulations of Alkaline Water Electrolyzers

S. Hess,[a] S. Zhang,[a] T. Kadyk,[b] W. Lehnert,[a,e] M. Eikerling,[b,c] and S. B. Beale[b,d]

[a]Institute of Energy and Climate Research, IEK-14, Forschungszentrum Jülich 52428 Jülich, Germany
[b]Institute of Energy and Climate Research, IEK-13, Forschungszentrum Jülich 52428 Jülich, Germany
[c]Chair of Theory and Computation of Energy Materials, Faculty of Georessources and Material Engineering,
RWTH Aachen University, Aachen, 52072, Germany
[d]Mechanical and Materials Engineering, Queen's University, Kingston ON K7L 3N6, Canada
[e]RWTH Aachen University, Faculty of Mechanical Engineering, 52062 Aachen, Germany

This study presents a computational simulation of a zero-gap alkaline water electrolysis cell. The model employed is a three-dimensional, steady-state, non-isothermal, two-phase-flow computational fluid dynamics approach, which has been implemented by means of the OpenFOAM software library. This integration expands the capabilities of the existing libraries within the open-source framework, openFuelCell2, by introducing novel surface and volumetric coupling strategies to connect the dependent quantities over the existing interfaces and different regions. Additionally, the Nernst–Planck equation is incorporated into the two-phase Eulerian–Eulerian framework to describe the behavior of the liquid electrolyte within the cell.
The model's validation in this study is based on experimentally-determined polarization curves for various temperatures and volumetric flow rates. The results obtained show good agreement with the experimentally-acquired data. The implemented model has demonstrated its ability to accurately predict the transport of ions within the electrolyte and assess the influence of the generated gas phase on the local distribution of current density.

Introduction

The extensive utilization of fossil fuels entails the large-scale emission of greenhouse gases and pollutants, necessitating the development of cleaner and sustainable energy alternatives. Amongst these, water electrolyzers have attracted significant attention, as they can directly convert electricity into chemical energy, offering one potential solution to this problem. Amongst the various types of electrolysis cells, the alkaline water electrolysis cell (AWE) has demonstrated noteworthy benefits. AWEs possess several advantages, including high efficiency, relatively low cost, and simplicity, primarily attributed to the utilization of non-precious metal catalysts like nickel and iron for the electrodes (1, 2).

Furthermore, the development of highly conductive, commercially-available diaphragms with a high bubble point, such as Zirfon® Perl UTP 500 (3, 4), and the reduction of ohmic resistance through the so-called zero-gap arrangement (5, 6), resulted in a significant increase in efficiency, even at higher current densities. Consequently, AWEs have found applications in various sectors, including large-scale stationary systems and hydrogen production powered by renewable energy (7). However, when AWEs have been powered by fluctuating renewable energy sources, gas impurities and the formation of a flammable gas mixture due to gas crossover between the anode and electrode sides has remained a major issue (8).

Understanding the impact of gas phase or gas bubble formation on the performance of alkaline electrolysis cells is a key area of investigation. However, experimental techniques such as neutron radiography (9) or synchrotron X-ray radiography (10), which visualize gas bubble formation in operational AWE cells, are challenging and have limited applicability. In contrast, employing multi-physical computational fluid dynamics (CFD) simulations of a three-dimensional (3-D) AWE cell can provide valuable insights into local behaviors and characteristics that are difficult or impossible to measure experimentally.

Ju et al. (11) introduced a 3-D CFD model capable of simulating a zero-gap cell and a two-phase flow coupled with electrochemical reactions. This model was further developed in (12) by implementing a non-homogeneous Euler–Euler mixture approach using the commercial Ansys Fluent software. Another 3-D CFD model for this cell type was proposed by Schimpalee et al., which employed a pseudo-two-phase flow model and emphasized the significance of a 3-D modeling approach in capturing geometry-dependent phenomena (13).

In this work, the openFuelCell2 library (14) which is integrated into the framework OpenFOAM, is extended for the special case of a zero-gap alkaline electrolyzer, taking charged species in the liquid electrolyte into account. The developed 3-D cell model can simulate the major physico-chemical hydrodynamic processes within the electrolyzer on a continuum scale. The model encompasses the description of various phenomena such as two-phase fluid flow, heat and mass transfer, electrochemical reactions, and species and charge transfer. In order to capture the behavior of each phase within the two-phase flow separately, an Eulerian–Eulerian approach, which accounts for interphase momentum transfer, is employed. In porous structures, the transfer of liquid water and the associated capillary pressure are modeled using the empirical Leverett J-function (15) approach. The model utilizes appropriate mapping functions and boundary conditions to establish coupling between geometrically-overlapping regions and parts.

Coupling strategy and numerical simulation

The simulation of an alkaline electrolyzer presents a complex and multi-physical problem that involves considerations of heat and mass transport, electrochemical reactions, momentum conservation, species transfer, and electrical potential. These phenomena are interdependent and, therefore, must be simulated in a coupled manner in order to accurately capture their interactions.

Geometry

Figure 1 displays a cross-section of the decomposed alkaline electrolysis cell, together with its components and coupling strategies. As in a physical cell, this model considers the bipolar plates (interconnect), flow fields (cathode/anode channels), electrodes (cathode/anode), and separator (diaphragm). Through decomposition of the computational domain, various sub-domains / regions are created. In each region and so on each mesh, different equations are solved simultaneously. The assumptions made and the governing equations solved in each of these regions are described below.

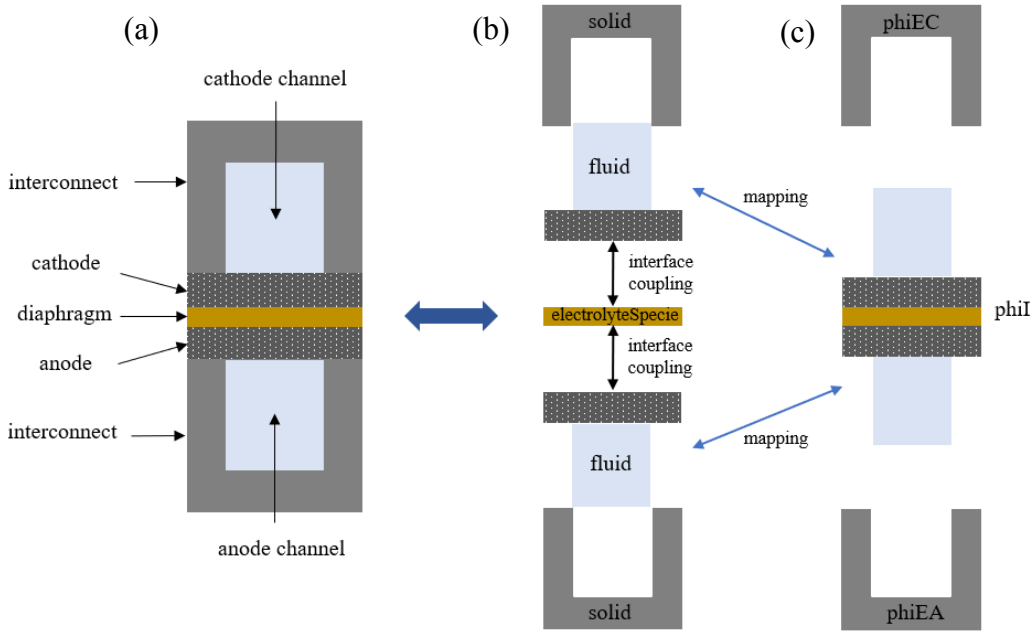

Figure 1. Components of the electrolyzer, computational domain, and decomposition: (a) main region; (b) fluid and solid regions; and (c) electrical/ ionic potential regions.

Assumptions

1. Simulations are for steady-state.
2. Flow of the gases and liquids is incompressible and laminar.
3. Gases behave like ideal gases.
4. The properties of the porous electrodes are homogeneous and isotropic.
5. Oxygen and hydrogen are produced in a gaseous state.
6. Diaphragm is impermeable to gas.
7. The liquid electrolyte is electroneutral at any point.
8. Electrolyte phase is highly diluted.
9. No interphase mass or heat transport.
10. No dissolved species within the liquid electrolyte.
11. Dispersed gas is treated as spherical bubbles.

Governing equations

For each region depicted in Figure 1, different transport equations are solved. For the *fluid* sub-regions, the modified Navier–Stokes equations for each phase, modified to include a darcy sink term, as well as the heat and species transport, including

electrochemical migration and the overpotentials, are calculated. The *electrolyteSpecie* region considers heat transfer and the transport of species inside the liquid electrolyte. The electric potential equations are solved in the regions *phiEA*, *phiEC*, and *phiI*. A global energy equation is solved in the *main* region. In this framework, the gas and liquid phases share the same pressure (apart from an algebraic term). Thus, the mixture continuity equation is inserted into the momentum equations to generate an equation to solve for the joint pressure. Numerically, the pressure–velocity coupling is conducted using a segregated Pressure-Implicit with Splitting of Operators (PISO) algorithm (16).

Fluid regions:

$$\frac{\partial}{\partial t}\left(s_q \rho_q\right) + \nabla \cdot \left(s_q \rho_q \boldsymbol{U_q}\right) = R_q \quad [1]$$

$$\frac{\partial}{\partial t}\left(s_q \rho_q \boldsymbol{U}_q\right) + \nabla \cdot \left(s_q \rho_q \boldsymbol{U}_q \boldsymbol{U}_q\right) = -s_q \nabla p + \nabla \cdot \left(s_q \mu_q \nabla \boldsymbol{U}_q\right) + s_q \rho_q g + \boldsymbol{M}_q + s_q S_{Darcy,q} \quad [2]$$

$$\frac{\partial(\rho_q s_q Y_i)}{\partial t} + \nabla \cdot \left(s_q \rho_q \boldsymbol{U}_q Y_i\right) = \nabla \cdot \left(s_q \rho_q D_i^{eff} \nabla Y_i\right) + \nabla \cdot \left(s_q u_i \rho_q Y_i \nabla \phi\right) + s_q R_{i,q} \quad [3]$$

$$\frac{\partial(s_q \rho_q h_q)}{\partial t} + \nabla \cdot \left(s_q \rho_q \boldsymbol{U}_q h_q\right) = \nabla \cdot \left(s_q \Gamma_q \nabla h_q\right) + s_q \dot{Q}_q \quad [4]$$

$$j_\mathrm{a} = exp\left[\frac{E_{a,a}}{R}\left(\frac{1}{T_{ref}} - \frac{1}{T}\right)\right] i_{\mathrm{a},0} s_l^{\gamma} \prod_\mathrm{i}\left[\exp\left(\frac{\alpha_\mathrm{a} z F \eta_\mathrm{a}}{R_g T}\right) - \exp\left(-\frac{(1-\alpha_\mathrm{a}) z F \eta_\mathrm{a}}{R_g T}\right)\right] \quad [5]$$

$$j_\mathrm{c} = exp\left[\frac{E_{a,c}}{R}\left(\frac{1}{T_{ref}} - \frac{1}{T}\right)\right] i_{\mathrm{c},0} s_l^{\gamma} \prod_\mathrm{i}\left[\exp\left(\frac{-\alpha_\mathrm{c} z F \eta_\mathrm{c}}{R_g T}\right) - \exp\left(\frac{(1-\alpha_\mathrm{c}) z F \eta_\mathrm{c}}{R_g T}\right)\right] \quad [6]$$

ElectrolyteSpecie region:

$$\frac{\partial(\rho_l s_l Y_i)}{\partial t} + \nabla \cdot \left(s_l \rho_l D_i^{eff} \nabla Y_i\right) + \nabla \cdot \left(s_l u_i \rho_l Y_i \nabla \phi\right) = 0 \quad [7]$$

Electric / ionic potential regions:

$$\nabla \cdot \left(\sigma_\mathrm{E} \nabla \phi_\mathrm{E}\right) = J_\mathrm{E} \quad [8]$$

$$\nabla \cdot \left(\sigma_\mathrm{I} \nabla \phi_\mathrm{I}\right) + \nabla \cdot \left(s_l z_{OH-} F D_{OH-}^{eff} \nabla C_{OH-}\right) = J_\mathrm{I} \quad [9]$$

Main region:

$$\frac{\partial(\rho C_p T)}{\partial t} + \rho C_p \boldsymbol{U} \cdot \nabla T = \nabla \cdot \left(k^{\text{eff}} \nabla T\right) + \dot{Q} \quad [10]$$

The ionic mobility is calculated via Nernst–Einstein equation (17) for diluted systems:

$$u_i = D_i^{eff} \frac{F z_i}{RT} \quad [11]$$

Coupled boundary conditions:

In both the *fluid* and the *electrolyteSpecies* regions, the species transport equations for OH-, K+, and H2O are solved. These equations are coupled across the corresponding interface via boundary conditions, with a Dirichlet condition at one side

$$Y_{i,left} = \xi Y_{i,right} \quad [12]$$

($\xi =$ 1 for no jump value) and a Neumann boundary condition accounting for the flux

$$\rho D_i^{eff} \nabla Y_i + s_l u_i \rho Y_i \nabla \phi = J \quad [13]$$

at the other side of the interface. Thus, the magnitude of the flux and the value for the mass fraction of the species must be equal.

Geometry and problem statement

The original geometry of the electrolyzer used in the experimental study is shown in Figure 2 (a) and together with the flow field in Figure 2 (b). In order to reduce the computational costs, the geometry has been simplified, as shown in Figure 2 (c). The resulting electrolysis cell has 14 parallel, straight channels and can be meshed using the *blockMesh* utility provided by OpenFOAM to generate a mesh consisting of 375,000 purely hexahedral cells.

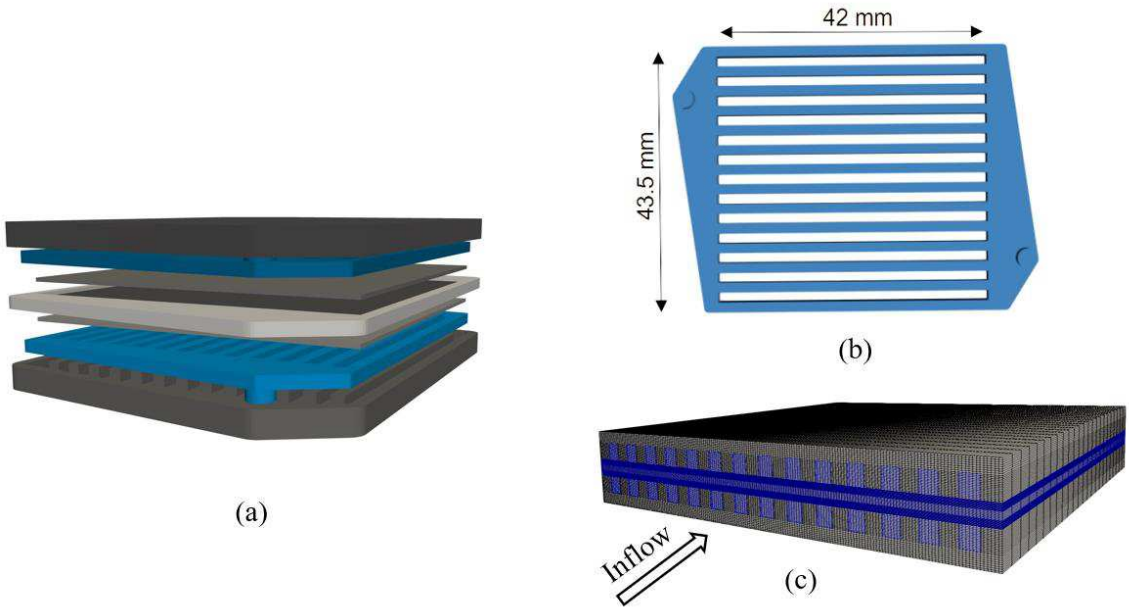

Figure 2. Geometry of the AWE cell used in the experiments (a) and the simplified computational domain (b).

Cell design and operating conditions

The porous electrodes were made of nickel and, for the diaphragm, Zirfon PERL UTP 500 (18) was used. The geometric properties, operating conditions, and model parameters for the electrolyzer from Figure 2 are listed in tables I, II, and III, below.

Table I. Geometry.

Description	Value
Channel height	1.5 mm
Channel width	1.5 mm
Rib width	1.5 mm
Number of channels	14
Cathode / Anode thickness	0.5 mm
Active surface area	18.27 cm^2
Diaphragm thickness	0.5 mm

Table II. Operating conditions.

Description	Value	Units
Pressure (anode and cathode)	101325	Pa
Inlet Temperatures	50 < T < 70	°C
Weight% KOH inlets	30	%
Liquid water saturation inlets	1	-
Volumetric flow rate	100	ml/s

Additionally, the material properties for the liquid electrolyte used in the simulations are summarized in the Appendix and consist of empirical formulations depending on the temperature and mass fraction of the potassium hydroxide solution.

Table III. Model parameters.

Description	Value	Units
Porosity electrodes (nickel foam)	0.96	-
Porosity diaphragm (Zirfon PERL UTP 500)	0.55 (18)	-
Bubble diameter	O2: 1.15e-04 H2: 2e-04	m
Diffusion coefficients electrolyte (reference T = 25°C)	OH-: 5.26e-09 (17) K+: 1.957e-09 (17) H2O: 2.272e-09 (12)	m^2/s
Permeability electrodes	1265914	m^2
Transfer coefficient	A: 0.4256 C: 0.3725	
Electric conductivity (solids)	1e06	S/m
Exchange current density (reference T = 25°C)	A: 9.3 (12) C:23.4 (12)	A/m^2

*A = anode, C = cathode

The alkaline electrolyzer in the simulation operates in galvanostatic mode, i.e., a specified mean current density is applied to the cell.

Results and discussion

The implemented solver has undergone successful testing on simpler geometries, such as cases without flow channels and those with a single channel. In these instances, the inlet conditions were adjusted to match the modified inlet surface. The presented results correspond to Figure 2 (c). Figure 3 illustrates a comparison between the simulation results and experimental data for the polarization curves at different temperatures, with a constant volumetric flow rate.

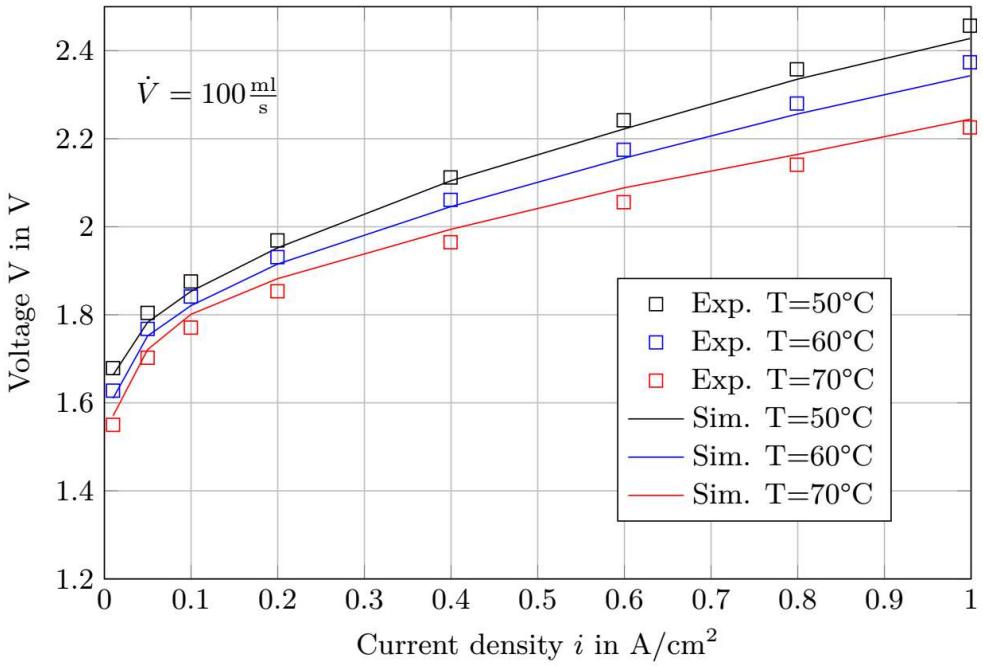

Figure 3. Polarization curves obtained by experiments and numerical simulations at different temperatures and a constant volumetric flow rate of $\dot{V} = 100\,\mathrm{ml/s}$.

The comparison between the experimental data and numerical simulations demonstrates a notable level of agreement, although the data used to describe the kinetics in particular are mainly taken from literature, i.e., they are not specifically measured for the electrodes used in the experiments. Further validation studies, employing the base of the openFuelCell2 framework, can be found in (19) for a different type of cell. Figure 4 displays the liquid water saturation evolution along the flow direction in the electrolyzer.

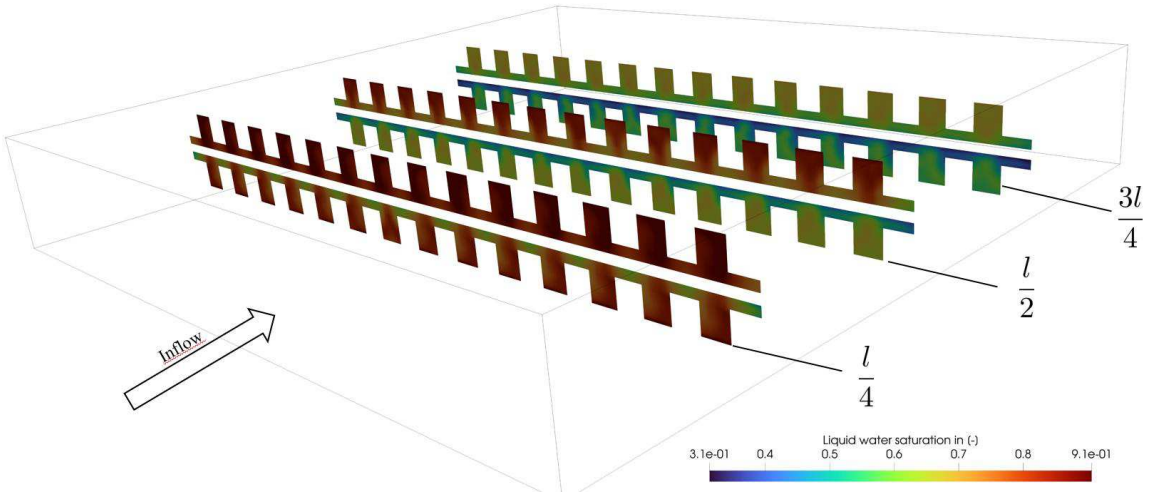

Figure 4. Liquid water saturation distribution at different cross-sections along the channels and within the electrodes for $i = 1\,\mathrm{A/cm^2}$.

Due to the production of gas in the form of oxygen and hydrogen on both the anode and the cathode sides, the liquid water saturation decreases in the flow direction. Furthermore, this decrease in liquid is larger on the cathode side, as for each transferred ion, twice the amount of hydrogen gas is produced in comparison to oxygen. It is also evident that the liquid saturation beneath the ribs is noticeably lower compared to that under the channels. This disparity arises due to the reduced convective transport that occurs under the ribs. This has an impact on the species concentration in the liquid electrode, which is depicted in Figure 5 for the hydroxide ions and the water molecules, as well. The left side of this figure displays the molar concentration of OH- in the first seven channels, whereas the right-hand side shows the molar concentration of water molecules in the remaining seven channels. Underneath the channels, the concentration in the porous electrodes closely matches that within the channels themselves. However, beneath the ribs, there is a noticeable variation in the concentration. Species that are consumed in the reaction exhibit a depletion, whereas those that are produced in the reaction demonstrate an accumulation.

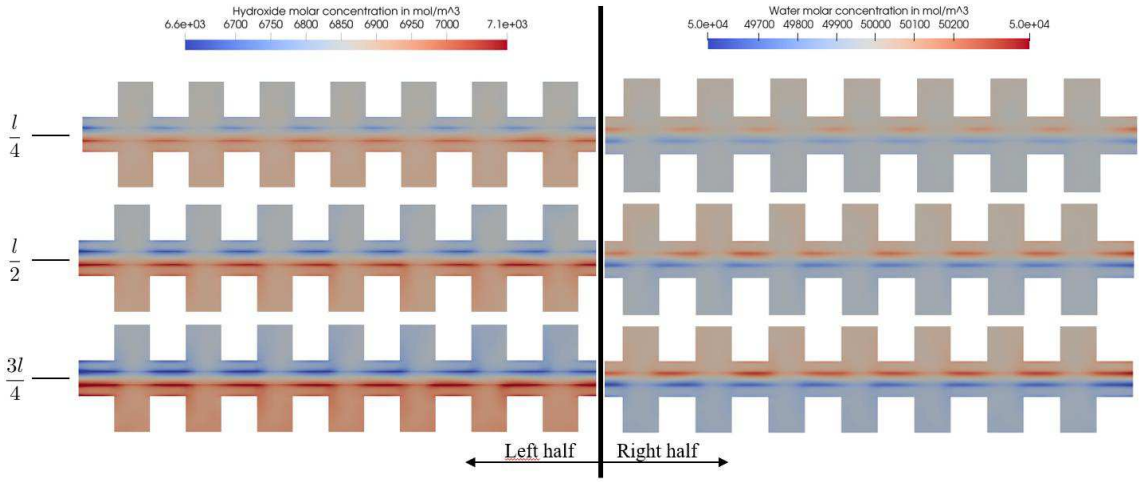

Figure 5. Distribution of the molar concentration of hydroxide ions (left) and water (right) in the electrolyte along the channels and within the electrodes for $i = 1\,\mathrm{A/cm^2}$.

Figure 6 (a) shows the current density distribution at the interface between the diaphragm and cathode. Its value is lower under the ribs and higher under the channels indicating the same trend for the liquid saturation shown in Figure 4 thereby illustrating the influence of saturation on current density, see equations [5] and [6]. One can notice a higher overpotential under the ribs and thus a decreased current density in these areas. In Figure 6 (b), it can be readily seen that a non-uniform distribution of the current density exists within the catalyst layer. The highest current density and therefore the highest reaction rates take place directly at the interface. Furthermore, the current density also decreases towards the outlet of the channel, which can also contribute to the increased gas saturation.

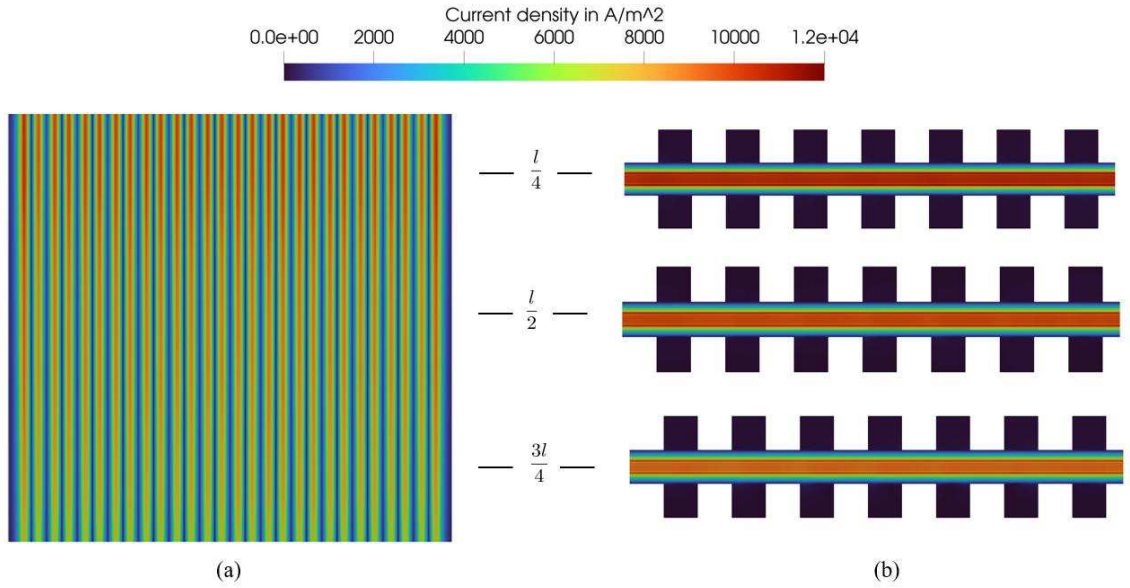

Figure 6. Current density distribution in the electrolyte at the interface between the anode and diaphragm (a) and along the channels and within the electrodes (b) for $i = 1\,\mathrm{A/cm^2}$.

Summary and future work

In this study, a 3-D, two-phase model for an AWE was implemented in the OpenFOAM library openFuelCell2. The model utilizes this approach to accurately capture the essential physical processes involved, including electrochemical reactions, as well as heat and mass transfer.

The model was applied to a 3-D simplified geometry of an in-house-developed, zero-gap AWE cell design. Based on data on the polarization curves for different temperatures and a constant volumetric flow rate gained from experiments, the model has been validated. For a wide range of current densities (up to 1 A/cm^2) the model predictions, in terms of polarization curves, shows good agreement with the experimental data. Moreover, the presented framework enables an examination of various factors, such as local variation in liquid saturation and its impact on the distribution of current density within the cell to be considered. This information serves as an indicator of the activity in different regions of the operational cell. By leveraging this knowledge, the cell's geometry can be optimized to enhance its performance.

In future, attention will be addressed to improvement of the numerical stability of the solution of the two-phase system and accelerate the convergence rate with a focus on the partial elimination algorithm and also on the implementation of consistent momentum interpolation techniques (20). Another issue that merits attention is the coupling of the species transport and the potential equation in the Nernst–Planck equation. An improved region-coupling approach for the species transport equation will also be applied.

Appendix

Material properties of the electrolyte solution

Density (21):

$$\rho_{KOH} = \left(K_1\left(T - T_{ref}\right)^2 + K_2\left(T - T_{ref}\right) + K_3\right)\exp(K_4 Y_{KOH})$$

$$K_1 = -3.25 \times 10^{-3}; \quad K_2 = 0.111; \quad K_3 = 1000; \quad K_4 = 0.86$$

Dynamic Viscosity (21):

$$\mu_{KOH} = \exp\left(K_{\mu_1} + K_{\mu_2}\left(T - T_{ref}\right) + K_{\mu_3}\left(T - T_{ref}\right)^2 + K_{\mu_4} Y_{KOH}\right)$$

$$K_{\mu_1} = 0.43; \quad K_{\mu_2} = -2.52 \times 10^{-2}; \quad K_{\mu_3} = 1 \times 10^{-4}; \quad K_{\mu_4} = 0.13$$

Specific heat capacity (21):

$$c_{p,KOH} = K_{c_{p,1}} + K_{c_{p,2}} \ln\left(K_{c_{p,5}}(T - T_{ref})/100\right) + \left(K_{c_{p,a}} + K_{c_{p,4}} * Y_{KOH} + 8K_{c_{p,6}}(T - T_{ref})\right) Y_{KOH}$$

$$K_{c_{p,1}} = 4.236 \times 10^3; \quad K_{c_{p,2}} = 1.075; \quad K_{c_{p,3}} = -4.831 \times 10^3; \quad K_{c_{p,4}} = 8;$$

$$K_{c_{p,5}} = 1; \quad K_{c_{p,6}} = 1$$

Heat conductivity (21):

$$\kappa_{KOH} = K_{\kappa_5}\left(K_{\kappa_1} + K_{\kappa_5}(T - T_{ref}) - K_{\kappa_3}(T - T_{ref})\right)^2 \left(1 - Y_{KOH}K_{\kappa_4}\right)$$

$$K_{\kappa_1} = 0.5545; \quad K_{\kappa_2} = 2.46 \times 10^{-3}; \quad K_{\kappa_3} = 1.184 \times 10^{-5}; \quad K_{\kappa_4} = 0.128;$$

$$K_{\kappa_5} = 1$$

Ionic conductivity (22):

$$\sigma_{KOH} = 100\left(\frac{\varepsilon}{\tau}\right)\left(K_{\sigma,1}M + K_{\sigma,2}M^2 + K_{\sigma,3}MT + K_{\sigma,4}(M/T) + K_{\sigma,5}M^3 + K_{\sigma,6}M^2T^2\right)$$

$$K_{\sigma,1} = -2.041; \quad K_{\sigma,2} = -2.8 \times 10^{-3}; \quad K_{\sigma,3} = 5.33 \times 10^{-3}; \quad K_{\sigma,4} = 207.2;$$
$$K_{\sigma,5} = 1.043 \times 10^{-3}; \quad K_{\sigma,6} = -3 \times 10^{-7}$$

Nomenclature

c_p	Specific heat capacity, J/kg/K
C	Molar concentration, mol/m^3
D	Diffusion coefficient, m^2/s
F	Faraday's constant, C/mol
$\boldsymbol{g}$	Gravity, m/s^2
h	Enthalpy, J/kg
k	Thermal conductivity, W/m/K
K	Constants
$\boldsymbol{i}$	Current density, A/m^3
i_0	Exchange current density, A/m^3
j	Current density, A/m^3
J	Current density source, A/m^3
ṁ	Mass flux, kg/m^2/s

$\boldsymbol{M}$	Interfacial momentum exchange term, J/kg
M	Molar mass, kg/mol / Molarity, mol/L
p	Pressure, Pa
$\dot{Q}$	Heat source, J/m^3
R	Mass source/sink, kg/m^3
s	Saturation
S	Darcy term, kg/m^2/s^2
T	Temperature, K
$\boldsymbol{U}$	Superficial velocity, m/s
u	Ionic mobility, As^2/kg
Y	Mass fraction

Greek symbols

α	Thermal diffusivity, m/s^2; transfer coefficient
ε	Porosity
γ	Saturation exponent
ϕ	Electrical potential, V
η	Activation overpotential, V
ρ	Density, kg/m^3
κ	Heat conductivity, W/mK
σ	Electric/ionic conductivity, S/m
J	Mass flux kg/m^2/s
μ	Dynamic viscosity, kg/m/s
τ	Tortuosity
ξ	Boundary jump

Subscripts

A	Anode
C	Cathode
E	Electronic charge
g	Gas
KOH	Potassium hydroxide
q	Phase
l	Liquid
OH-	Hydroxide ion
P	Protonic/ionic charge

Superscripts

eff	Effective

Acknowledgments

The work presented here was partially supported by AIDAS – AI, Data Analytics and Scalable Simulation – which is a Joint Virtual Laboratory gathering at the Forschungszentrum Jülich (FZJ) and the Alternative Energies and Atomic Energy Commission (CEA), France.

Special thanks go to Stefanie Renz from the IEK-14 of the FZJ for providing the experimental data.

References

1. Sergey A. Grigoriev, Vladimir N. Fateev, Pierre Millet, *Comprehensive Renewable Energy (Second Edition)*, *Elsevier,* 459-472 (2022)
2. O. Schmidt, A. Gambhir, I. Staffell, A. Hawkes, J. Nelson, S. Few, *Int. J. Hydrog. Energy,* **42**(52), 30470-30492 (2017)
3. P. Vermeiren, W. Adriansens, R. Leysen, *Int. J. Hydrog. Energy,* **21**(8), 679–684 (1996)
4. P. Vermeiren, J.P. Moreels, R. Leysen, *J. Porous Mater.,* **3**, 33-40 (1996)
5. J.W. Haverkort, H. Rajaei, Journal of Power Sources, **497**, 0378-7753 (2021)
6. C. Dunninill and R. Phillips, *RSC Adv*., **6**, 100643-100651 (2016)
7. J. Brauns and T. Turek, *Processes,* **8**(2), 248 (2020)
8. Y. Xia, H. Cheng and W. Wei, *Commun. Eng.,* **22**, 2731-3395 (2023)
9. O. Panchenko, E. Borgardt, W. Zwaygardt, F. J. Hackemüller, M. Bram, N. Kardj lov, T. Arlt, I. Manke, M. Müller, D. Stolten, and W. Lehnert, *Journal of Power Sources,* **390**, 108 - 115 (2018)
10. M. A. Hoeh, T. Arlt, I. Manke, J. Banhart, D. L. Fritz, W. Maier, W. Lehnert, *Electrochemistry Commun.,* **55**, 55-59 (2015)
11. J. Hyunchul, A. Afroz, L. Jaeseung, *Int. J. Hydrog. Energy,* **46**(26), 13678-13690 (2021)
12. J. Hyunchul, A. Afroz, L. Jaeseung, C. Park, S. Yoon, *Fuel,* **315**, 0016-2361 (2022)
13. S. Shimpalee, S-G. Kang, J.S Lopata, H-S. Cho, C-H. Kim, J.W. Weidner, *Electrochimical Acta,* **390,** 0013-4686 (2021)
14. S. Zhang, S. Hess, H. Marschall, U. Reimer, S.B. Beale and W. Lehnert, *openFuelCell2: A New Computational Tool for Fuel Cells, Electrolyzers, and other Electrochemical Devices and Processes, Computer Physics Communications,* (2023) in preparation
15. K. S. Udell, *International Journal of Heat and Mass Transfer,* **28**(2), 485 – 495 (1985)
16. R. I. Issa, *Journal of Computational Physics,* **62**(1), 40 - 65 (1986)
17. J. Newman, K. Thomas-Aylea, *Electrochemical Systems Third Edition*, p. 672, John Wiley & Sons, Inc., Hoboken, New Jersey (2012)
18. Agfa, Technical Data Sheet ZIRFON PERL UTP 500, (2020)
19. S. Zhang, S. B. Beale, Y. Shi, H. Janßen, U. Reimer and W. Lehnert, *ECS Trans.*, **98** (9), 317-329 (2020)
20. N. Fueyo, A. Cubero, A. Sanchez-Insa, *Computers and Chemical Engineering,* **62**, *96– 107* (2014)
21. P. Mandin, D. Le Bideau, M. Kim, M. Sellier, *Int. J. Hydrog. Energy*, **44**(10), 4553-4569 (2019)
22. A. Hodges, S. Renz, F.Lohmann-Richters, A. Al-Musawi, A. Jupke, W. Lehnert, G. F. Swiegers, and G. G. Wallace, *Journal of Chemical & Engineering Data*, **68**(7), 1485-1506 (2023)